UARS MLS Cloud Ice Measurements and Implications for H_2O Transport near the Tropopause

D. L. Wu[1], W. G. Read[1], A. E. Dessler[2], S. C. Sherwood[3], and J. W. Waters[1]

Date: October 22, 2003

Submitted to *J. Atmos. Sci.*

1. Jet Propulsion Laboratory, California Institute of Technology, Pasadena, California
2. Earth System Science Interdisciplinary Center, University of Maryland, College Park, Maryland
3. Department of Geology and Geophysics, Yale University, New Haven, CT

Key words: Cloud ice, Microwave remote sensing, tropospheric tropopause

Corresponding author address: Dr. Dong L. Wu, M/S 183-701, Jet Propulsion Laboratory, California Institute of Technology, 4800 Oak Grove Drive, Pasadena, CA 91109. Email: Dong.L.Wu@jpl.nasa.gov

Abstract

A technique for cloud detection and Ice Water Content (*IWC*) retrieval is described here and applied to UARS MLS (Upper Atmosphere Research Satellite Microwave Limb Sounder) 203-GHz radiance measurements at tangent pressures between 300 and 46 hPa. At these tangent pressures the radiances remain optically thin and cloudy-sky radiances are brighter than normal clear-sky cases. Unlike infrared/visible cloud observations, the 203-GHz radiances are sensitive mostly to large ice crystals that are often of convective origin rather than thin cirrus. The initial MLS *IWC* results and comparisons with MLS water vapor measurements reveal many interesting features in the tropical tropopause layer (TTL) region. The 100-hPa *IWC* averaged between 30°S-30°N is approximately constant at ~0.07 mg/m^3, or 0.7 ppmv for equivalent water vapor at this pressure, but large *IWC*s are concentrated over convective centers where seasonal mean ice content can exceed 20 ppmv vapor equivalent. The correlation between *IWC* and water vapor at 100 hPa is relatively poor over oceans compared to one over land masses. However, there exists good correlation between tropical *IWC* and RH_i (relative humidity with respect to ice) at 100 hPa during both the dry (January-March) and moist (July-September) periods.

1. Introduction

Clouds near the tropopause play a potentially important role in the water budget in the Earth's upper troposphere. However, lack of cloud and water vapor measurements has been a major limitation in our understanding of what this role is. In particular, the role of overshooting, convective clouds near the tropical tropopause has been contested in the literature (e.g., Newell and Gould-Stewart 1981; Danielsen 1982; Dessler 1998; Sherwood and Dessler 2000; Holton and Gettelman 2001).

Measuring cloud ice at the tropopause altitudes has been one of the most difficult challenges for remote sensing from space. Passive nadir-viewing microwave techniques cannot sufficiently resolve the vertical distribution of cloud ice at tropopause heights. These observations have been limited to the measurements of cloud liquid water path (*LWP*) and ice water path (*IWP*) (e.g., Evans et al. 1998; Liu and Curry 2000; Zhao and Weng 2002). Satellite infrared (IR) and visible limb-scan techniques (e.g., Wang et al., 1995) can only measure ice properties in the uppermost cloud layers (particularly, thin cirrus) but fail for ice mass associated with deep convective systems.

Millimeter and sub-millimeter limb techniques offer a new opportunity for cloud observations in the upper troposphere and are complementary in many aspects to IR/visible sensors. For example, microwave limb techniques provide higher vertical resolutions than nadir-viewing sensors at these frequencies, and the cloud ice measurement is insensitive to cloud top temperature or surface emission. At microwave frequencies, radiation can penetrate through most ice clouds and yield information on large or massive ice particles inside clouds. These properties, particularly useful for

inferring cloud ice water content (*IWC*), are not limited by multiple scattering and cloud inhomogeneity that often cause problems in other remote sensing techniques.

This paper describes and applies a cloud detection and retrieval technique to the UARS MLS (Upper Atmosphere Research Satellite Microwave Limb Sounder) 203-GHz radiances at tangent heights near the tropopause. The preliminary results of *IWC* and occurrence frequency reveal several interesting features in the dry (January-March 1992) and wet (July-September 1992) phases of the "tape recorder" phenomenon in the lowermost tropical stratosphere (Mote et al. 1996). We show that the 100-hPa MLS radiance is proportional to *IWC* at this height and can be used to monitor variations of the tropopause cloud ice. Because MLS provides nearly collocated measurements for cloud ice and water vapor (Read et al. 2003) at 100 hPa, these data are especially valuable for studying STE in the TTL region where the dynamics are still considerably influenced by tropospheric processes with large temporal and spatial variabilities.

2. MLS 203-GHz Observations

a. UARS MLS Experiment

UARS MLS is a passive instrument with three double-sideband radiometers near 63, 183 and 203 GHz, measuring temperature, H_2O, O_3 and ClO profiles in the middle atmosphere (Barath et al. 1993; Waters 1993; Froidevaux et al. 1996; Livesey et al. 2003). There are 30 spectral channels in the 183-GHz radiometer and 45 channels in the 203-GHz radiometer that cover spectral ranges: 183.1-186.5 GHz and 200.1-206.4 GHz, respectively. Compared to nadir-scanning operational microwave radiometers, the vertical field-of-view (FOV) of the MLS 203-GHz radiometer is narrower: ~3 km at the

tangent point. The horizontal resolutions are 7 km across and ~300 km along the line-of-sight (LOS).

The MLS scanning plane is 90° from the satellite direction of motion and the antenna step-scans the atmospheric limb from ~90 km to the surface in 65.5 s during normal operation. The scan interval varies from ~3 km at tangent heights in the stratosphere/troposphere to ~5 km in the mesosphere. MLS radiances lack coherence when they hit clouds because the spatial separation between adjacent measurements is too large (vertically by ~3 km and horizontally by 15 km). Such sparse spatial sampling cannot adequately resolve deep convective clouds that are mostly sensed by MLS. The MLS horizontal resolution is limited by the smearing along the LOS (~300 km). MLS latitudinal coverage ranges from 34° in one hemisphere to 80° in the other as a result of the 57° orbital inclination and the instrument viewing direction. UARS performs a 180°-yaw maneuver 10 times per year to allow alternate observations of high latitudes every ~36 days. The MLS 203-GHz radiometer was fully operational (producing ~1300 profiles per day) between September 1991 and December 1994 before the number of daily profiles was reduced. The 183-GHz radiometer stopped collecting data in April 1993 after 18 months of successful operation. Beside the normal scan mode, MLS was also operated occasionally with a limb-tracking mode in which the FOV points at a fixed tangent height (usually ~18 km).

The MLS 183- and 203-GHz radiometers together provide nearly-collocated water vapor and cloud ice in the UT/LS (upper troposphere and lower stratosphere) region. The 183-GHz radiances have best sensitivity to water vapor in the lower stratosphere (Pumphrey 1999) and in the upper TTL region (Read et al. 2003). On the

other hand, the 203-GHz channel provides the best water vapor sensitivity at 464-147 hPa (Read et al., 2001). However, these water vapor retrievals suffer from cloud contamination when scattering of ice particles is strong. Cloud-induced radiances are best detected with the 203-GHz channel and can be used for cloud ice retrieval.

b. Cloud Signatures in Limb Radiances

Clouds can affect MLS radiances at all tangent heights below the cloud top but cloud effects vary substantially with frequency and tangent height. The best channel for cloud detection is near the spectral window (i.e., 203 GHz for MLS) where the radiances are least affected by H_2O and O_3. Figure 1 shows MLS radiance measurements at ~203 GHz during limb-scan and limb-tracking operations. In the limb-scan case [Figure 1a], clear-sky radiance profiles are mostly clustered in a narrow band with clear upper and lower bounds. Temperature and water vapor variabilities cause the radiance spread within the band. A few measurements outside the clear-sky band are indicative of thick-and-dense clouds where the cloud-induced radiance ΔT_{cir} (the difference from the clear-sky limit) can be as much as 30 K at ~12 km tangent height and -130 K below 5 km. The instrument noise (~0.09 K for each 2-s measurement at 203 GHz window channels) is generally negligible compared to these cloud effects. Between 8 and 12 km, cloud effects are difficult to distinguish from clear-sky variability. Thus, for microwave limb observations, clouds are detectable only when limb radiances are either optically thin (at high tangent heights) or optically thick (at low tangent heights), and this paper is focused on the cloudy radiances in optically-thin cases.

During the 18-km limb-tracking [Figure 1(b)], clear and cloudy radiances can be distinguished by their very different horizontal correlation lengths. Clear-sky radiances vary smoothly along the orbit as tangent pressure, water vapor and temperature change, except for the sharp discontinuities due to adjustments in MLS pointing. Clouds at this tangent height manifest themselves as large point-to-point radiance perturbations of much shorter horizontal scales. At this tangent height, ΔT_{cir} can reach as much as 20 K above the background and shows poor point-to-point coherence. Because adjacent measurements are separated by ~15 km horizontally, MLS measurements of cloud radiance are likely to be uncorrelated since MLS is primarily sensitive to deep convective clouds, which have spatial scales < 15 km at these altitudes.

Both ice emission and scattering can give rise to excess radiances at tangent heights above ~12 km. In the emission case, cloud ice is similar to gas species producing additional thermal radiation on the top of other atmospheric emissions. In the scattering case, cloud ice particles scatter radiation into MLS FOV and cause the net brightness temperature to increase from the clear-sky background. Because the clear-sky background is normally small (20-50 K) at high tangent heights, cloud scattering tends to bring more radiation into than out of the MLS FOV. For both ice emission and scattering cases, the excess radiance ΔT_{cir} can be converted to *hIWP* (total ice content in the path along the MLS LOS) using modeled ΔT_{cir}-*hIWP* relations. However, it is not practical to invert *hIWP* to obtain the *IWC* profile on a single scan because of insufficient sampling with the MLS scan. Most retrieving techniques assume spherical homogeneous layers, which is not valid for MLS samples that are separated horizontally by ~15 km and vertically by ~3 km. To overcome this limitation, we first make regional averages on the

hIWP data to obtain variabilities of monthly or seasonal scales, and then retrieve *IWC* from the regionally-averaged *hIWP* (using Abel inversion). A similar approach was used on SAGE II (Stratospheric Aerosol and Gas Experiment II) data to retrieve profiles of cloud occurrence frequency (Wang et al. 1995).

c. Clear and Cloudy-Sky Separation

The methods for cloud detection generally fall into two categories: (i) empirical approaches based on clear-cloudy sky contrasts among adjacent measurements, and (ii) model approaches to determine clear-sky limits thought a radiative-transfer (RT) model. In either case, a practical cloud detection algorithm needs to be robust and reliable enough to handle various circumstances such as missing data and poor knowledge about atmospheric state and instrument pointing. Unlike IR limb sounding cases where the challenge is to separate between clouds and aerosols (Kent et al. 1993), the goal for MLS is to best distinguish clouds from other clear-sky variabilities (such as those due to water vapor and temperature).

In this study we choose to use the RT model method for cloud detection. If a measured radiance is greater or less than the modeled clear-sky limits (e.g., 110% RH_i), it is flagged as a cloud-sky measurement and the difference (observed-modeled) is the cloud-induced radiance. The RT model we use here is described in Read et al. (2001) and initialized with MLS v5 temperature, tangent pressure, stratospheric water vapor and ozone retrievals. For the calculations of the clear-sky limits, we assume that air is saturated with 110% relative humidity with respect to ice in the troposphere (below 100 hPa).

Figure 2 shows ΔT_{cir} extracted from the data in Figure 1a with the RT method. In this paper, we focus on cloudy cases at tangent pressures less than 300 hPa, which give positive ΔT_{cir}. There is a sharp division between the numbers of measurements with ΔT_{cir} greater and less than zero at pressures less than 200 hPa, indicating that the RT model method works reasonably well in separating clear-sky (negative ΔT_{cir}) and cloudy-sky (positive ΔT_{cir}) radiance measurements. The division between clear and cloudy sky cases starts to blur at pressures between 200-300 hPa, reflecting the increasing error with the RT model. The model uncertainty is typically 3-5 K at 100-200 hPa, mostly due to temperature, pointing and spectroscopic errors, and for reliable cloud detection we set $\Delta T_{cir} > 3$ K as the criterion for positive identification of cloud hits.

3. Cloud Ice Retrieval

Figure 3 outlines the MLS upper tropospheric cloud ice detection and retrieval algorithm scheme. In this algorithm the clear-sky RT model is used to extract ΔT_{cir} from the radiance measurements and the cloudy-sky RT is used to find the ΔT_{cir}-*hIWP* relations needed in cloud ice retrieval. Unlike the conventional definition of cloud ice column, *hIWP* is the integral along the MLS LOS and oriented more horizontally than vertically.

a. ΔT_{cir}-hIWP relation

The ΔT_{cir}-*hIWP* relations are calculated using a full RT model with cloud scattering (see more model descriptions in *Appendix A*). In addition to the assumptions for particle size and shape, we use a cloud profile model between 5-17 km where *IWC* decreases exponentially (~4-km scale height) with height. Because the 203-GHz radiation

can penetrate most thick-and-dense clouds at tangent pressures less than 200 hPa, the ΔT_{cir}-*hIWP* relations are only slightly affected by the assumed *IWC* profile shape. To correct for cloud self-extinction and air attenuation, we weight the *IWC* contribution to *hIWP* with the transmission function such that clouds beyond the radiation penetration depth contribute little to the limb radiance. This correction is generally not significant at high tangent heights because of weak cloud self-extinction and clear-sky attenuation. However, this correction becomes very important for the radiances at low tangent heights. In the case of strong attenuation, *hIWP* represent a measurement over a partial LOS path.

Each ΔT_{cir} must first be converted to *hIWP* on a single limb measurement before the individual measurements are averaged into a monthly or seasonal composite. As shown in Figure 4 the calculated ΔT_{cir}-*hIWP* relation varies with tangent height, from ~7 K kg^{-1} m^2 at ~15 km to ~11 K$kg^{-1}m^2$ at 11 km, and depends on the particle size distribution (PSD) assumed in the model. We use the height-dependent PSD parameterization by McFarquhar and Heymsfield (1997), and calculate the slope of the ΔT_{cir}-*hIWP* relation for each tangent height used later by the cloud ice retrieval. It is important to point out that the PSD-dependent ΔT_{cir}-*hIWP* relation is the major error source in MLS cloud ice retrieval. Especially for deep convective clouds, which are poorly represented in the in-situ PSD database used by McFarquhar and Heymsfield (1997), ice particles can be strongly mixed among altitudes, and reliable size and shape representations are difficult to obtain. Our estimate of the accuracy is ~200% in the ΔT_{cir}-*hIWP* relation mostly due to the PSDs assumed (see more in the Discussion section).

b. IWC Retrievals

The individual *hIWP*(z_t) at tangent pressure z_t are averaged and interpolated into 8 tangent pressure bins (44.4, 58.2, 76.3, 100, 131, 172, 225, and 296 hPa) and 5°x10° (latitude × longitude) grids. The 5°×10° bin size gives typically ~40 MLS samples in the tropics during one month or ~120 profiles during one season. *IWC* is then retrieved from the *hIWP*s on four pressure levels at 76, 100, 131, and 172 hPa in each latitude-longitude grid using the *onion-peeling* technique. A 3-K uncertainty is estimated for the ΔT_{cir} measurements, mostly due to the RT model error, which yields ~5 mg/m^3 uncertainty in *IWC* at 100 hPa. The threshold for the minimum detectable cloud is also 3 K, which provides good confidence on cloud detection. A lower threshold can falsely flag many clear-sky cases and introduce variabilities not associated with clouds.

The retrieved *IWC* is a regional mean of cloud ice under both clear and cloudy sky conditions. There is an important difference between the mean *IWC* and the mean single-cloud *IWC* in the region. The latter is the *IWC* averaged only for cloudy cases, which measures average ice mass carried by a cloud. These two quantities are related by cloud occurrence frequency, a quantity that can be also derived from MLS 203-GHz radiance, but is an average over an MLS footprint which is likely to be only partially cloud-filled.

c. IWC - ΔT_{cir} Relation at 100 hPa

Because most deep convective clouds in the tropics top out around 100 hPa, the inversion from *hIWP* to *IWC* is generally not needed at this level, and the 100-hPa ΔT_{cir} is approximately proportional to *IWC* at 100 hPa. Our model calculations [Figure A.2] show

that the *IWC* - ΔT_{cir} relation at 100 hPa is nearly linear for ΔT_{cir} less than ~30 K with a slope of ~1.5 mg/m^3/K for the PSD parameterization in McFarquhar and Heymsfield (1997). Since MLS cloud-induced radiance measurements are mostly less than 30 K at this level, we can simply use the linear portion of the *IWC*-ΔT_{cir} relation for the conversion at 100 hPa. Like the *hIWP*-ΔT_{cir} conversion, the *IWC*-ΔT_{cir} conversion is subject to large uncertainties due to the PSD assumption.

4. Initial Results

We will focus on the dry (January-March) and moist (July-September) phases of the lower stratospheric "tape recorder" (Mote et al. 1996). Figures 5 and 6 compare maps of temperature, cloud occurrence frequency, *IWC*, water vapor and relative humidity at 100 hPa for the two periods in 1992. MLS v702 water vapor (Read et al. 2003) is used to help diagnose/interpret *IWC* morphology. These water vapor data have the best sensitivity at 215-46 hPa with a 3-km vertical resolution. The *RH*i is derived from MLS H_2O volume mixing ratio (*vmr*) and NCEP temperature. The following analyses are focused on the geographical distribution and temporal variation of cloud ice in relation to temperature, water vapor, and relative humidity with respect to ice (*RH*i) at 100 hPa.

a. Dry Period (January-March 1992)

During the dry period the 100-hPa *IWC* has clear maximums near the intertropical convective zones (ITCZ), along with the cloud occurrence frequency. The map of occurrence frequency agrees well with overshooting cloud morphology observed by the TRMM Precipitation Radar (Alcala and Dessler 2002). The maximum 100-hPa *IWC* in this seasonal average reaches ~3 mg/m^3, which coincides with the peak of the cloud

occurrence frequency (~20%). Deep convective regions over South America and South Africa have less ice mass at 100 hPa with a maximum of ~2 mg/m^3 in *IWC* and ~20% in frequency. Over northern Australia and the southeast Asian archipelagos, there are some scattered occurrences with *IWC* around 1-1.5 mg/m^3.

The comparison with NCEP temperature shows that the cold (less than 196 K) regions are associated with the high 100-hPa *IWC*s but shifted slightly in latitude. Generally speaking, the region with temperature less than 198 K exhibits good symmetry about the equator and covers a larger area than cloud ice. Despite the shift in latitude, the longitudinal temperature variations (2-4 K) correlate well with the *IWC* ones. The longitudinal correlation and latitudinal symmetry with temperature is also present in comparisons between MLS *IWC* with UKMO (UK Met Office) temperature (not shown).

At 100 hPa the *IWC* patterns differ noticeably from the H_2O *vmr*, especially in the southern subtropical Pacific where the high *vmr* belt is ~5-10° southward of the *IWC* band. This shift between these two maximum locations implies the water vapor band is even farther away from the center of the cold temperature region in the central Pacific. The vapor *vmr* and cloud ice distributions at 100 hPa appear to have larger deviation over oceans than over land masses. However, the 100-hPa *IWC* patterns are found to correlate significantly better with MLS 147-hPa vapor *vmr* (not shown) and no obvious latitudinal shift is found between the 100-hPa *IWC* and 147-hPa *vmr* maximums in the southern Pacific.

In the Northern Hemisphere, there exists a low (~2.3 ppmv) H_2O *vmr* band around ~25°N latitude across most longitudes with a slightly wider region over the Central America. This low *vmr* band also exists but appears wider at 147 hPa where the

moist band in the Southern Hemisphere shrinks and vanishes eventually at 215 and 316 hPa (not shown). The similar H_2O distribution repeats during the period of January-March 1993. Over South America and South Africa, *IWC* and H_2O *vmr* are well correlated but the locations of their maximums remain slightly shifted.

There is a better correlation between the *IWC* and RH_i patterns at 100 hPa. However, some differences do exit. For example, the peak RH_i is found slightly north of the *IWC* maximum over South America, but aligned closely over South Africa. Interestingly, the 100-hPa RH_i over the central Pacific is lower than those over land masses, whereas the opposite is true for the 100-hPa *IWC* for land-ocean differences. This appears in line with the finding of Sherwood (2002) that continental cumulus clouds have smaller crystal sizes, which would reduce their microwave scattering potential but increase their ability to moisten the tropopause region. However, caution is required when interpreting relative humidity here since it depends on NCEP temperatures. The average RH_i is far below saturation at 100 hPa near the cloudy regions, varying between 25% and 40%, which is mostly due to the biases in MLS H_2O retrieval and NCEP temperature. MLS water vapor retrieval is found to have a low bias at 100 hPa (Read et al. 2003), whereas the NCEP temperature is known to have a warm bias (Randel et al. 2000), which we have not attempted to correct here. Because the seasonally-averaged RH_i includes both clear and cloudy cases, the value should be less than 100% in general.

b. Moist Period (July-September 1992)

During the moist period [Figure 6], the 100-hPa *IWC* pattern is dominated by the contributions from Indian monsoons and typhoon systems in Southeast Asia. Deep

convective systems produce up to an 8 K difference in NCEP temperature cross the latitude band at ~25°N. The UKMO temperature data suggest similar but somewhat smaller (4-6 K) perturbations at this latitude band (not shown). Again, the region with 100-hPa temperature lower than 200 K covers most of the tropics and subtropics, and is centered on the equator at most latitudes. The cold region is strongly perturbed by the Asian and American monsoons, pushing the envelope north to ~40ºN. Like in the dry period, longitudinal temperature variations seem well correlated with *IWC*.

Compared to the Asian monsoon, the Central American monsoon contributes much smaller *IWC* at 100 hPa. A similar amount of contribution is found over central Africa and western Pacific. Unlike in the dry period, the correlation between *IWC* and H_2O *vmr* at 100 hPa is generally good in most places, particularly near the Indian and Central American monsoons, showing peaks of 3 mg/m^3 in *IWC* and ~5 ppmv in H_2O *vmr*. Away from the deep convective zones, there is no obvious dry latitude band in the Southern Hemisphere (winter hemisphere) where the *vmr* decreases monotonically with latitude.

Overall, *IWC* in the wet period correlates better with RH_i at 100 hPa than with the other fields. The monsoons over India/Asia, Central America and Africa produce RH_i of 25-40% at 100 hPa with the highest RH_i over Indian/Asian region. There are strong latitudinal RH_i and temperature gradients north of the Indian monsoon as deep convective activity pushes far north from the equator. The cloud ice maximums over Japan, Central America and Africa coincide with high RH_i, but not necessarily with peak RH_i values. This lends to further indication that the ice is primarily convective, rather than formed in

situ according to RH_i, although another possibility is that aerosol lofted to high levels localizes in situ cloud formation by heterogeneous nucleation.

c. Seasonal Variations

The temporal behavior of MLS cloud ice and water vapor is dominated by seasonal variations, and is strongly latitude-dependent, as shown in Figure 7. Here, the 100-hPa *IWC* and water vapor data are limited to the early period of UARS mission (September 1991 - April 1993) when both MLS 183- and 203-GHz radiometers were operating.

The seasonal cycle of MLS 100-hPa cloud radiance (as a cloud ice proxy) resembles that of deep convective activity in the middle troposphere, varying around the equator within ±10° in latitude. The cloud ice variation is consistent with MLS H_2O *vmr* at 147 hPa as expected for the moistening from convective outflows at the bottom of the TTL. However, the latitudinal spread of the 147-hPa H_2O is slightly wider than that of the cloud ice at 100 hPa, which may be interpreted as a result of evaporation of ice and advection of moist air.

The seasonal variation of the 100-hPa *vmr* differs substantially from that of the 100-hPa cloud ice. This level is affected both by convection (Dessler 2002) and by the stratospheric circulation (Yulaeva et al 1994), and the *vmr* seasonal cycle reflects variations in both of these processes. The interactions between convection and synoptic circulations in the UT/LS region are complex, and depend on many variables, such as microphysical properties of the clouds as well as ambient relative humidity (Sherwood 2002; Sherwood and Dessler 2003; Dessler and Sherwood 2003). A comprehensive

explanation and quantification of the distribution of these variables will have to await further theoretical and observational studies.

The moisture variation exhibits a very different pattern when expressed in RH_i instead of *vmr*. Because of the strong dependence of RH_i on temperature, most of the RH_i variations result from the latitudinal and seasonal variations of temperature. The temperature error must be considered seriously in this analysis because of nonlinearity of the Clausius-Clapeyron equation. A 1-K error in temperature would yield a relative error of 17% in RH_i at 100 hPa, and therefore, conclusions based on RH_i variations should be treated with caution.

d. Interannual Variation of Tropical Tropopause Clouds

Cloud ice variability near the tropical tropopause is summarized in the time series of the daily averaged 100-hPa ΔT_{cir} (ΔT_{cir}=0 if it is clear sky) between 30°S and 30°N. This average reflects a balance of total ice mass at 100 hPa between supply from deep convection and sedimentation by gravity. We focus on long-term variations of the daily averaged ΔT_{cir} because short-term variabilities are too complicated to interpret due to MLS insufficient sampling. To ensure the quality of the averages, we interpolate the radiances to 100 hPa and exclude the days with less than 200 measurements in the tropics (30°S-30°N).

Figure 8 shows the time series of daily ΔT_{cir} and the daily cloud occurrence frequency during 1991-1997. Over this 5½ year period, the 100-hPa ΔT_{cir} is maintained at a level of ~0.05 K, corresponding to an *IWC* of 0.075 mg/m^3 (using the PSD described in section 3). This *IWC* amount is equivalent to 0.75 ppmv H_2O *vmr* at 100 hPa globally,

representing a significant but not dominant portion of the total H_2O budget at this level. In addition, the cloud occurrence frequency, which mostly represents clouds of deep convective origin, is maintained at a level of 1-2% over the years. The interannual and seasonal variations in ΔT_{cir} are not significant compared to uncertainties in the cloud detection method and threshold.

The cloud occurrence frequency exhibits a long-term variation that is significant at 100 hPa and more pronounced at 130 hPa. The frequency of cloud occurrence is lower around 1994 and higher in 1991 and 1997. Such variation is also evident in MLS 215- and 147-hPa water vapor (Kley et al. 2000), and the cause of this interannual variation remains to be investigated.

5. Discussion

MLS 203-GHz radiances can provide useful measurements of cloud ice content and occurrence frequency of convective clouds in the UT/LS region with higher vertical resolution than those from nadir-viewing instruments. Because of the penetrative ability of microwave radiation, the 203-GHz limb radiance has a sufficient dynamic range to measure the ice content associated with thick-and-dense clouds, in particular, those from deep convection. Also because of the penetrative ability, cloud inhomogeneity along the LOS becomes less a problem than in optically-saturated cases. In other words, the *hIWP*-ΔT_{cir} relation remains same regardless where clouds are placed along the LOS.

The MLS cloud ice measurements represent mostly deep convective clouds, which are beyond, and therefore complementary to, the capability of IR and visible techniques. Mie scattering calculations (assuming the McFarquhar-Heymsfield PSD) suggest that most of the sensitivity at 200 GHz comes from ice particles of 100-300 μm.

This is much larger than sizes expected in subvisible cirrus formed in situ (Jensen et al. 1996), but is typical for deep convective cores where the updraft velocity is strong enough to lift large particles. This inference is also consistent with the observed localization of the ice distribution relative to that of relative humidity, and with the large ice mixing ratios inferred.

We showed in this study that limb radiance perturbations due to deep convective clouds can be extracted with good confidence using a clear-sky radiative transfer model. By allowing some model errors and clear-sky variabilities, we can detect the cloud-induced radiance for ΔT_{cir}> 3 K at 100 hPa. The 100-hPa clear-sky background is typically around 20 K at 203 GHz, and about 5-10% of the measured ΔT_{cir} are greater than 3 K.

Large uncertainty arises when converting MLS cloud-induced radiances to *IWC* because the assumptions about ice particle size and shape distributions. PSD serves as a key link between the ice masses sensed by MLS and those insensible by MLS (such as thin cirrus). Because MLS 203-GHz radiances are only sensitive to ice particles of the large-size mode, the inferred *IWC* is quite sensitive to the shape of the PSD. Many PSD parameterizations produce a distribution shape that is height dependent and sometimes *IWC* dependent like in McFarquhar and Heymsfield (1996).

Table 1 summarizes the 100-hPa *IWC* converted from the same ΔT_{cir} using different PSDs, and the result can differ by a factor of 2-3. The size distribution used in our retrieval (i.e., McFarquhar and Heymsfield 1997) was developed from aircraft observations of deep convective outflows during the Central Equatorial Pacific Experiment (CEPEX). This parameterization is able to produce the bimodal distribution

for large *IWC* clouds and has taken into account some measurements near the tropopause. However, it lacks the inputs from situations inside convective cores. Due to strong turbulence/mixing of the updraft, the PSD inside convective cores may differ substantially from those measured in the outflows. Strong overshooting cases can yield updraft velocities as high as 20 ms^{-1} (e.g., Geerts et al., 2000), with which ice particles can be readily mixed over several km. As a result, deep convective clouds at 100 hPa may have a PSD similar to those at lower altitudes. As shown in Table 1, the results from the PSDs at -60°C and -75°C differ by 30%, which is relatively small compared to the PSDs from different parameterizations.

The PSD shapes vary substantially among different parameterizations. Liu and Curry (1998) studied essentially the same CEPEX data and determined a different parameterization for PSD. The primary difference between McFarquhar-Heymsfield and Liu-Curry parameterizations is in the assumption for particles of diameter less than 100 μm. The Liu-Curry parameterization produces a smaller mass-mean diameter for the same temperature and hence a larger MLS *IWC*. Heymsfield et al. (2002) compiled a parameterization from the in-situ measurements of ice particle sizes from field campaigns in tropical and subtropical regions at temperatures mostly warmer than -55°C. Their parameterization is formulated in terms of gamma distributions as a function of altitude. The MLS *IWC* from the -60°C PSD in this case gives the same result as one using the McFarquhar and Heymsfield PSD despite different mass-mean diameters. The result from the -75°C PSD in Heymsfield (2002) may be negligible because it is simply an extrapolation from the measurements at lower altitudes. Overall, there are not many reliable in-situ observations of PSDs at temperatures less than -70°C, and even fewer

in/near convective cores. Lack of reliable particle size information under these situations means that the uncertainty of MLS 100-hPa *IWC* might be as high as 100-200%.

In addition to the uncertainties associated with the PSD, Evans and Stephens (1995) also argued that ice particle shapes could cause *IWC* retrieval error by a factor of 2 under extreme conditions. Hence, reducing uncertainties associated with particle size and shape remains as a major challenge in future cloud observations.

Finally, cloud occurrence frequency from limb observations can differ significantly with those from nadir techniques due to resolution issues and cloud detection method. Lowering the detecting threshold would generally increase cloud occurrence frequency but also increase the probability of false detection. In the MLS case, the increase of the false detection would add some water vapor variability to cloud ice field and degrade the cloud measurements severely. Effects of partially-filled footprints on cloud occurrence frequency are complicated. Differences between nadir- and limb-viewing cases depend on cloud and footprint sizes as well as radiances induced by each individual cloud, and more quantitative studies are needed to carry out these differences.

6. Summary

Our initial *IWC* retrievals, together with MLS water vapor measurement and NCEP temperature data, reveal many interesting features related to interactions between deep convective clouds and tropopause dynamics. These results can be summarized as follows:

1. The patterns of MLS *IWC* generally correlate positively with the water vapor *vmr* at 100 hPa except near the southern Pacific during the dry period (e.g., January-March

1992), where the *vmr* peak is located 5-10° south of the *IWC*. Better agreement is found when comparing the 100-hPa *IWC* to the 147-hPa H_2O *vmr*.

2. The average 100-hPa *IWC* between 30°S-30°N is ~0.07 mg/m^3 during 1991-1997, which is obtained assuming the McFarquhar and Heymsfield (1997) PSD in cloud scattering calculations. This *IWC* gives a global ~0.7 ppmv for equivalent water vapor at 100 hPa, a significant portion of the total water budget in the tropical tropopause. Seasonal *IWC* means may reach up to 30 ppmv vapor equivalent over convective areas, far exceeding the vapor mass at this level. However, these *IWC* values must be treated with caution since there is an uncertainty of factor of 2-3 due to possible PSD error.
3. We are not able to identify significant seasonal or inter-annual variations in the daily averages of the tropical ΔT_{cir} but there are possible long-term variations in cloud occurrence frequency during 1991-1997. The variation in cloud occurrence frequency is more noticeable at 130 hPa than at 100 hPa, showing the lowest occurrence frequency in 1994.
4. There is a generally good correlation between *IWC* and RH_i at 100 hPa in both seasonal extremes. However, ice distributions are more localized but often offset from RH_i maxima, suggesting that deep convection is the dominant source of the observed local RH_i variability, as expected from radiative transfer arguments. Ice maxima over land areas tend to be moister than those over oceans, suggesting dynamical or microphysical differences between the cloud systems.

A new MLS instrument, to be launched on NASA Aura satellite in 2004, will use the similar limb observing technique but with more frequencies (118, 190, 240, 640 GHz

and 2.5 THz), broader bandwidths and high sampling rates (every ~0.4 km in tangent height) to study the UT/LS region (Waters et al. 1999). Significant improvements are expected for MLS water vapor and cloud ice observations over the TTL region, which will help to resolve some issues not adequately addressed with the UARS data.

Acknowledgments

We thank Dr. Gloria Manney for providing the NCEP and UKMO temperature data and Dr. Jonathan Jiang for helping with some cloud model descriptions and simulations. AED and SCS acknowledge an EOS Interdisciplinary Science grant to the University of Maryland and Yale University. This research was performed at the Jet Propulsion Laboratory, California Institute of Technology, under contract with the National Aeronautics and Space Administration (NASA).

Appendices

Appendix A. Cloudy-sky radiative transfer (RT) model

The RT model that we use to calculate MLS 203-GHz cloudy radiances is briefly described in the following. The radiative transfer equation we solve along the LOS can be written as

$$\frac{dT_b}{ds} = -\beta_e T_b + \beta_a \hat{T} + \beta_s T_{scat} \qquad (1)$$

where s is distance along the LOS, T_b is microwave radiance in Kelvin, and β_e, β_a, and β_s are total volume extinction, absorption and scattering coefficients, respectively, in unit of m^{-1} (e.g., Ulaby *et al.* 1981). The first source function $\hat{T}$ represents emission and is equal to atmospheric temperature T under the Rayleigh-Jeans approximation. The second source function T_{scat} accounts for the radiances scattered into the LOS by clouds. For simplicity, we neglect the polarization properties of cloud scatterers, and assume spherical ice particles. The atmosphere is divided into spherically-stratified layers with vertically-varying gas and cloud variables (temperature, density, ice water content, etc.).

Equation (1) can be evaluated by separate downward and upward integrals. For the *downward* path, the integration is carried out from the top of model atmosphere to the tangent point (or the surface if the tangent height is below the surface), and the *upward* path integration is carried out from the tangent point (or the surface) to the top of the atmosphere.

We assume that the scattering processes are independent (or incoherent) among different cloud hydrometers, which is valid at microwave frequencies, so that the total scattered radiances can be expressed as the sum of contributions from different particles (van de Hulst, 1981). Cloud ice particles are assumed made of pure water with density ρ_{ice}= 0.91 g/cm^3. Mie theory is applied to calculate phase functions and scattering coefficients for each particle size. The model ice PSD (particle size distribution) uses the parameterization described in McFarquhar and Heymsfield (1997) and is divided into 40 size bins between 0-4000 μm in diameter.

The source functions T_{scat} are calculated using an iterative approach at each cloud layer (e.g., Wilheit et al, 1982). Figure A.1 illustrates the coordinates to calculate T_{scat} under a layered atmosphere, where the scattering volume is placed at the origin, the Z-axis is zenith, and the LOS lies in the Y-Z plane with angle Θ from zenith and Φ=90° from X-axis. The incident radiance T_b with zenith angle Θ′ is a function of θ, ϕ and Θ, where angles (θ, ϕ) are the angular coordinates with respect to the LOS. Since the incident T_b is only a function of Θ′ if the atmosphere is layered, the expression for T_{scat} can be simplified to the following

$$T_{scat}(\Theta) = \frac{1}{2}\int_0^{\pi} P(\theta')\overline{T}_b(\theta')\sin\theta' d\theta' \qquad (2)$$

and

$$\overline{T}_b(\theta') = \frac{1}{2\pi}\int_0^{2\pi} T_b(\theta', \phi')d\phi'$$
$$= \frac{1}{2\pi}\int_0^{2\pi} T_b(\Theta')d\phi'$$

where θ' is the scattering angle between Θ and Θ' and ϕ' is the azimuth angle that lies in the plane perpendicular to the LOS. The angle Θ' can be expressed in terms of θ', ϕ' and Θ as

$$\cos\Theta' = \vec{r} \cdot \vec{z} = \sin\theta' \sin\Theta \sin\phi' + \cos\theta' \cos\Theta$$

where $\vec{r}$ and $\vec{z}$ are respectively the unit vectors of the incident radiance and the zenith directions. $\overline{T}_b(\theta')$ is evaluated at each layer for all zenith angles Θ' from the surrounding radiation. For the angular integrations, the model uses 16 θ-streams and 8 ϕ-streams on 0.125-km vertical grids. This configuration produces less than 1% error in the 200 GHz limb radiances under typical convective clouds.

Iterations for the T_{scat} calculation start by first initializing all the *downward* radiances to 0 K and all the *upward* radiances to 300 K. From these radiances T_{scat} are evaluated using Eq.(2) and then substituted into Eq.(1) to produce a new set of *downward* and *upward* radiances. The next iteration now starts with the new radiances, and the final T_{scat} is obtained if convergence (0.1 K) is found. All the source functions are then used in the definitive radiative transfer calculation along the limb path.

References

Alcala, C.M., and A.E. Dessler, 2002: Observations of deep convection in the tropics using the TRMM precipitation radar, *J. Geophys. Res.*, **107** (D24), 4792, DOI: 10.129/2002JD002457.

Barath, F., et al., 1993: The Upper Atmosphere Research Satellite Microwave Limb Sounder instrument, *J. Geophys. Res.*, **98**, 10,751-10,762.

Danielsen, E. F., 1982: A dehydration mechanism for the stratosphere, *Geophys. Res. Lett*., **9**, 605-608.

Dessler, A. E., 1998: A reexamination of the "stratospheric fountain" hypothesis, *Geophys. Res. Lett*., **25**, 4165-4168.

_____, 2002: The effect of deep, tropical convection on the tropical tropopause layer, *J. Geophys. Res*., **107** (D3), 4033, DOI: 10.1029/2001JD000511.

_____, and S.C. Sherwood, 2003: Does convection hydrate or dehydrate the upper troposphere/lower stratosphere region?, manuscript in preparation.

Evans, K. F., and G. L. Stephens, 1995: Microwave radiative transfer through clouds composed of realistically shaped ice crystals. Part I: Single scattering properties. *J. Atmos. Sci*., **52**, 2041-2057.

_____, et al., 1998: Modeling of submillimeter passive remote sensing of cirrus clouds. *J. Appl. Meteor.*, **37**, 184-205.

Froidevaux, L., et al., 1996: Validation of UARS Microwave Limb Sounder ozone measurements. *J. Geophys. Res*., **101**, 10,017-10,060.

Geerts, B., et al., 2000: Hurrican Georges' landfall in the Dominican Republic: Detailed airborne Doppler radar imagery, *Bull. Am. Meteor. Soc.*, **81**, 999-1018.

Heymsfield, A. J., et al., 2002: Observations and parameterizations of particle size distributions in deep tropical cirrus and stratiform precipitating clouds: Results fron In-situ observations in TRMM field campaigns, *J. Atmos. Sci.*, **59**, 3457-3491.

Holton, J. R., et al., 1995: Stratosphere-Troposphere exchange, *Reviews of Geophysics*, **33**, 4, 403-439.

_____, and A. Gettelman, 2001: Horizontal transport and dehydration in the stratosphere, *Geophys. Res. Lett*., **28**, 2799-2802.

van de Hulst, H. C., 1981: *Light Scattering by Small Particles*. Dover, 470 pp.

Jensen, E. J., et al., 1996: On the formation and persistence of subvisible cirrus clouds near the tropical tropopause. *J. Geophys. Res* **101** (D16): 21361-21375.

Kent, G. S., D. M. Winker, M. T. Osborn, and K. M. Skeens, 1993: A model for the separation of cloud aerosol in SAGE II occultation data, *J. Geophys. Res.*, **98**, 20,725-20,735.

Kley, D., J. M. Russell III, and C. Phillips, 2000: SPARC assessment of upper tropospheric and stratospheric water vapour, *SPARC Report* **No. 2** WCRP-113, WMO/ICSU/IOC, CNRS, Verriere le Bruisson.

Liu, G., and J. A. Curry, 1998: Remote sensing of ice water characteristics in tropical clouds using aircraft microwave measurements. *J. Appl. Meteor*., **37**, 337-355.

_____, and J. A. Curry, 2000: Determination of ice water path and mass median particle size using multichannel microwave measurements. *J. Appl. Meteor*., **39**, 1318-1329.

Livesey, N.J., et al., 2003: "The UARS Microwave Limb Sounder version 5 dataset: Theory, characterization and validation", *J. Geophys. Res*., in press.

Madden, R. A., and P. R. Julian, Seasonal variations of the 40-50 day oscillation in the zonal wind in the tropical Pacific. J. Atmos. Sci., 28, 702-708, 1971.

McFarquhar, G. M., and A. J. Heymsfield, 1997: Parameterization of tropical cirrus ice crystal size distributions and implications radiative transfer: Results from CEPEX. *J. Atmos. Sci.*, **54**, 2187-2200.

Mote, P. W., et al., 1996: An atmospheric tape recorder: The imprint of tropical tropopause temperatures on stratospheric water vapor. *J. Geophys. Res.*, **101**, 3989-4006.

Newell, R. E., and S. Gould-Stewart, 1981: A stratospheric fountain?, *J. Atmos. Sci.*, **38**, 2789-2796.

Oltmans, S.J., and D.J. Hofmann, 1995: Increase in lower-stratospheric water vapour at a mid-latitude northern hemisphere site from 1981 to 1994. *Nature*, **374**, 146-149.

Pumphrey, H. C., 1999: Validation of a new prototype water vapor retrieval for the UARS Microwave Limb Sounder, *J. Geophys. Res.*, **104**, 9399-9412.

Randel, W.J., F. Wu, and D. J. Gaffen, 2000: Interannual variability of the tropical tropopause derived from radiosonde data and NCEP reanalyses. *J. Geophys. Res.* **105** 15509-15523.

_____, et al., 2001: Seasonal variation of water vapor in the lower stratosphere observed in Halogen Occultation Experiment data, *J. Geophys. Res*., **106**, 14,313-14,325.

Read, W. G., et al., 2001: UARS MLS upper tropospheric humidity measurements: Method and validation, *J. Geophys. Res.* **106** (D23): 32207-32258.

_____, D. L., Wu, J. W. Waters, and H. C. Pumphrey, 2003: A new 147-68 hPa water vapor product from the UARS Microwave Limb Sounder. submitted to *J. Geophys. Res*.

Rosenlof, K.H., et al., 2001: Stratospheric water vapor increases over the past half-century, *Geophys. Res. Lett*., **28**, 1195-1198.

Sherwood, S. C., 2002: A microphysical connection among biomass burning, cumulus clouds, and stratospheric moisture. *Science*, **295**, 1272-1275.

_____, and A. E. Dessler, 2000: On the control of stratospheric humidity. *Geophys. Res. Lett*., **27**, 2513-2516.

_____, and _____, 2003: Convective mixing near the tropical tropopause: Insights from seasonal variations, *J. Atmos. Sci*., accepted.

Ulaby, F. T., Moore, R. K., and Fung, A. K., 1981: *Microwave Remote Sensing: Active and Passive, Volume I: Microwave Remote Sensing Fundamentals and Radiometry*, Artech House, Inc. 456 pp

Wang, P.-H., et al., A method for estimating vertical distribution of the SAGE II opaque cloud frequency. *Geophys. Res. Letts*., **22**, 243-246, 1995.

Waters, J. W., 1993: Microwave limb sounding. Atmospheric Remote Sensing by Microwave Radiometry. M. A. Janssen, Ed., John Wiley and Sons, Inc., 572 pp., 1993.

_____, et al., 1999: The UARS and EOS Microwave Limb Sounder Experiments. J. Atmos. Sci., **56**, 194-218.

Wilheit, T. T., et al., 1982: Microwave radiometric observations near 19.35, 95 and 183 GHz of precipitation in tropical storm Cora, *J. Appl. Meteorol*., **21**, 1137-1145.

Yulaeva, E., J.R. Holton, and J.M. Wallace, 1994: On the cause of the annual cycle in tropical lower-stratospheric temperatures, *J. Atmos. Sci*., **51** (2), 169-174.

Zhao, L., and F. Weng, 2002: Retrieval of ice cloud parameters using the Advanced Microwave Sounding Unit, *J. Appl. Meteor*., **41**, 384-395.

Table

Table1 The average 100-hPa *IWC* converted from MLS 203-GHz ΔT_{cir} using different PSDs. The differences reflect uncertainties in current PSD parameterizations in the upper troposphere, which in turn limits the accuracy of MLS IWC retrieval. D_{mm} is mass-mean diameter, weighted by the cubic power of particle diameter.

	T (°C)	D_{mm} (μm)	IWC (mg/m^3)
McFarquhar and Heymsfield [1997]	-60	114	0.056
	-75	103	**0.075**
Heymsfield et al., [2002]	-60	143	0.056
	-75	73	0.201
Liu and Curry [1998]	-60	64	0.123
	-75	56	0.171

Figure Captions

Figure 1. UARS MLS 203-GHz radiances measured during (a) limb-scan and (b) limb-tracking operations. In the limb-scan case, most of the radiances are confined in the envelopes determined by clear-sky variability. Above ~12 km tangent heights clouds are indicated by excess radiances above the clear-sky limit, whereas at lower tangent heights they show up as radiance depressions below the clear-sky limit. Clouds are not readily detectable at intermediate tangent heights (8-12 km for 203 GHz). In the limb-tracking case, clear- and cloudy-sky radiances show very different variations in terms of horizontal scale. The large short-scale radiance fluctuations near 20°N-25°N are indicative of cloud hits, whereas the more gradual radiance variations are likely due to water vapor and pointing variations. The periodic discontinuities along the orbit are caused by pointing corrections in maintaining 18-km limb tracking.

Figure 2. Cloud-induced radiances as determined with the RT method, which can reach as large as 60 K at tangent pressures less than 300 hPa. The imbedded box indicates the cloudy cases of interest to this study. The RT method works reasonably well at tangent pressures up to ~200 hPa but become less useful in the middle troposphere.

Figure 3. MLS cloud ice retrieval scheme.

Figure 4. *hIWP*-ΔT_{cir} relations for 203-GHz limb radiance as calculated from the cloudy-sky RT model. The model uses the PSD parameterization in McFarquhar and Heymsfield (1997) and assumes spherical ice particles for scattering calculations. The calculated *hIWP*s have been corrected for cloud self-extinction and air attenuation effects (see the text).

Figure 5. Cloud ice, water vapor and temperature maps at 100 hPa for January-March 1992. Top: MLS cloud occurrence frequency (colors) and NCEP temperature (contours). Middle: MLS *IWC*

(colors) and H_2O *vmr* (contours). Bottom: MLS *IWC* (colors) and RH_i (contours). Profiles contaminated by clouds are excluded in the water vapor and RH_i maps.

Figure 6. As in Figure 5 except for July-September 1992.

Figure 7. The time series of (a) 100-hPa MLS cloud radiance, (b) 146-hPa MLS H_2O *vmr*, (c) 100-hPa MLS H_2O *vmr*, and (d) 100-hPa MLS RH_i,. The cloud radiance is used to estimate *IWC* variations at 100 hPa. As described in section 3, the radiance can be approximately converted to 100-hPa *IWC* using the factor of 0.15 mg/m^3/K. For the 100-hPa H_2O *vmr* and *RHi* results, cloudy profiles are excluded from the averaging. The white strips represent missing data. In the *RHi* time series, sudden increases/decreases in value are likely the retrieval errors as *RHi* becomes very sensitive to temperature uncertainty at this level.

Figure 8. Average (30°S-30°N) MLS cloud radiances at 100 and 130 hPa tangent pressures during 1991-1997. Daily averages are plotted in small dots whereas the 30-day running averages are represented by large dots. Interpolation is applied to obtain the values at 100 and 130 hPa. Data are excluded if the number of measurements is less than 200 in the latitude bin.

Figure A.1 Diagram to illustrate the geometry of cloud scattering calculation in the limb RT model.

Figure A.2. Calculated *IWC*-ΔT_{cir} relation at 100 hPa. The dotted line shows the slope of 1.5 mg/m^3/K in the linear portion of the *IWC*-ΔT_{cir} relation.

Figure 9. UARS MLS 203-GHz radiances measured during (a) limb-scan and (b) limb-tracking operations. In the limb-scan case, most of the radiances are confined in the envelopes determined by clear-sky variability. Above ~12 km tangent heights clouds are indicated by excess radiances above the clear-sky limit, whereas at lower tangent heights they show up as radiance depressions below the clear-sky limit. Clouds are not readily detectable at intermediate tangent heights (8-12 km for 203 GHz). In the limb-tracking case, clear- and cloudy-sky radiances show very different variations in terms of horizontal scale. The large short-scale radiance fluctuations near 20°N-25°N are indicative of cloud hits, whereas the more gradual radiance variations are likely due to water vapor and pointing variations. The periodic discontinuities along the orbit are caused by pointing corrections in maintaining 18-km limb tracking.

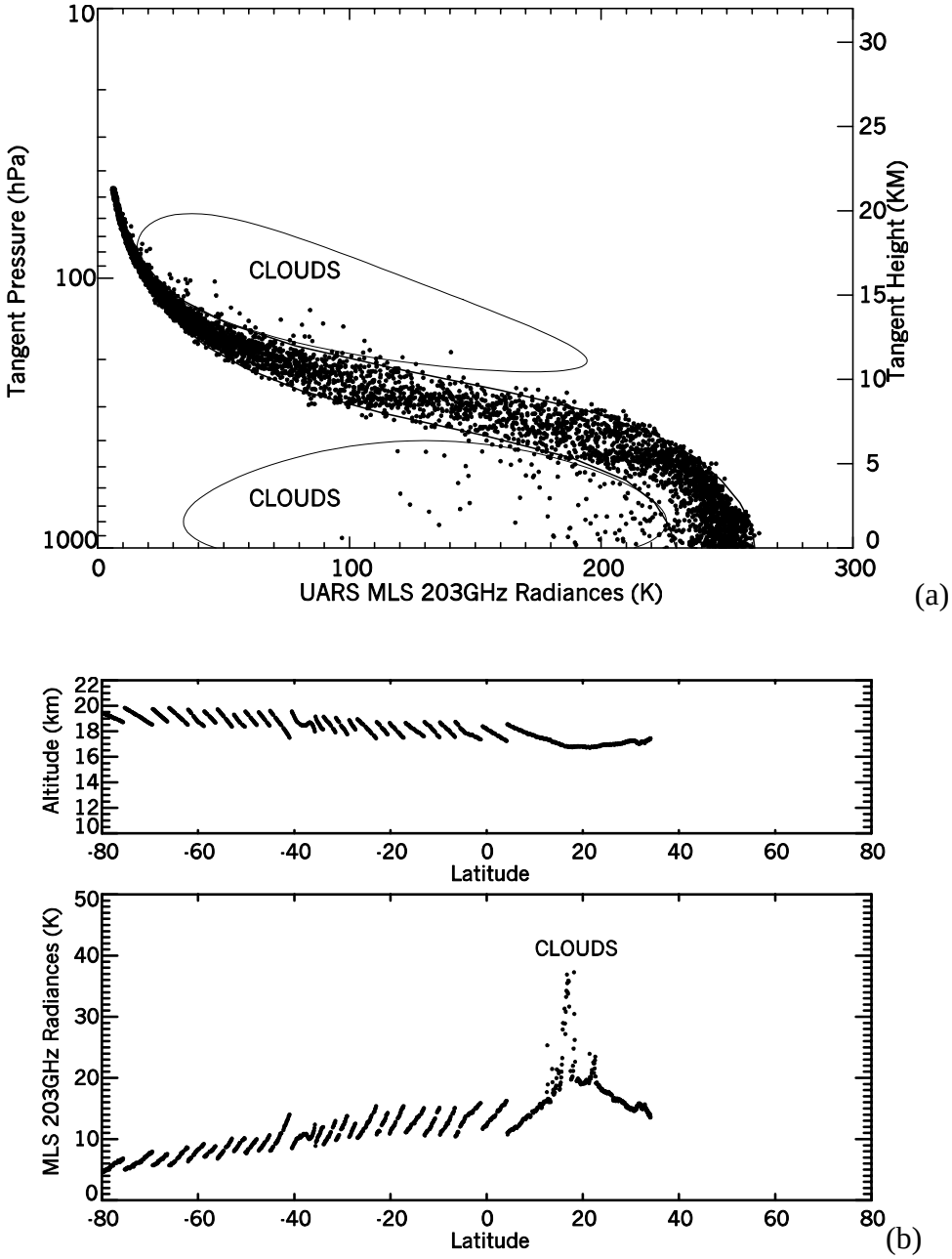

Figure 10. Cloud-induced radiances as determined with the RT method, which can reach as large as 60 K at tangent pressures less than 300 hPa. The imbedded box indicates the cloudy cases of interest to this study. The RT method works reasonably well at tangent pressures up to ~200 hPa but become less useful in the middle troposphere.

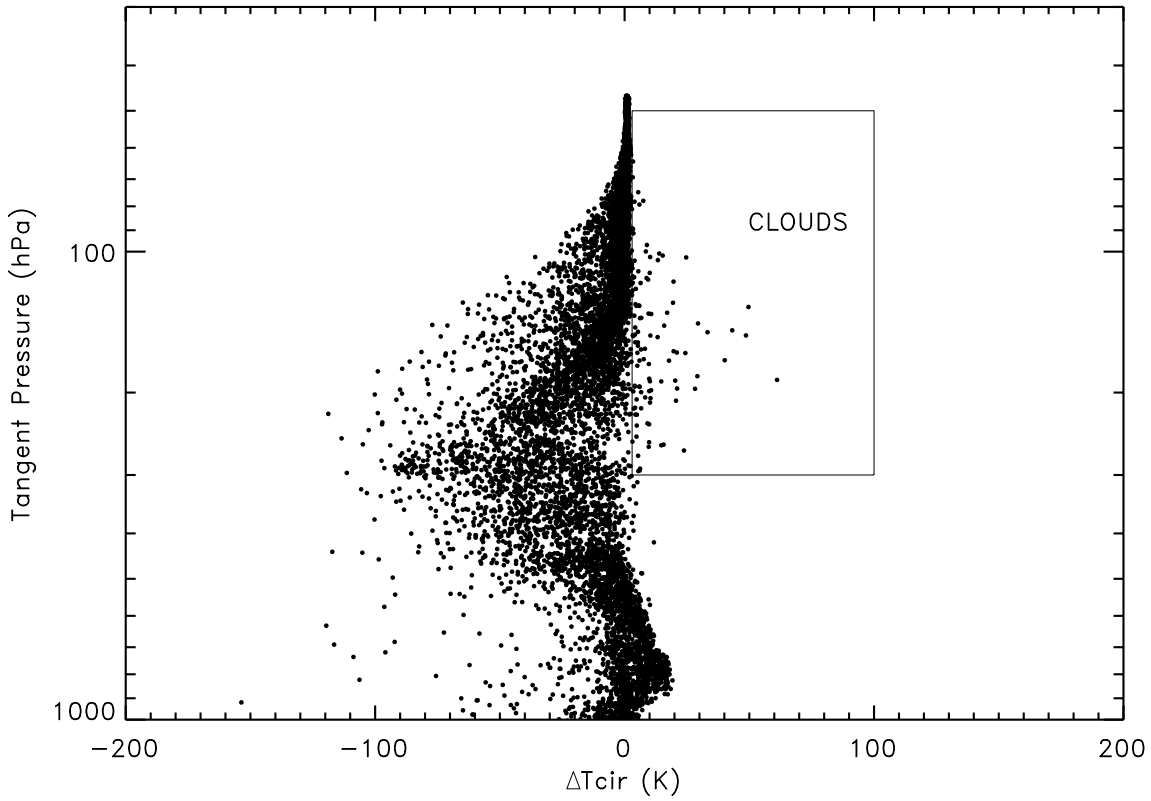

Figure 11. MLS cloud ice retrieval scheme

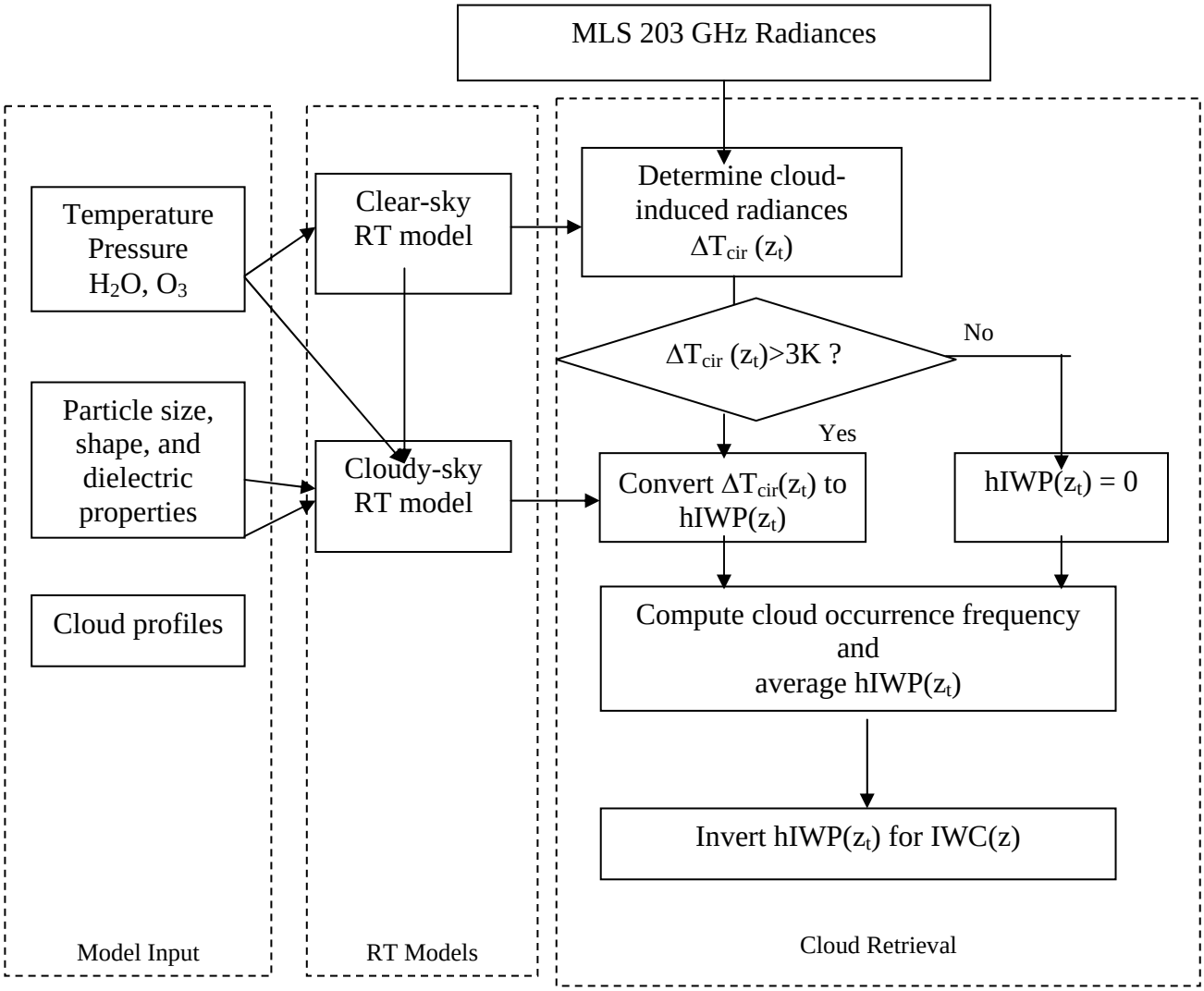

Figure 12. *hIWP-*ΔT_{cir} relations for 203-GHz limb radiance as calculated from the cloudy-sky RT model. The model uses the PSD parameterization in McFarquhar and Heymsfield (1997) and assumes spherical ice particles for scattering calculations. The calculated *hIWP*s have been corrected for cloud self-extinction and air attenuation effects (see the text).

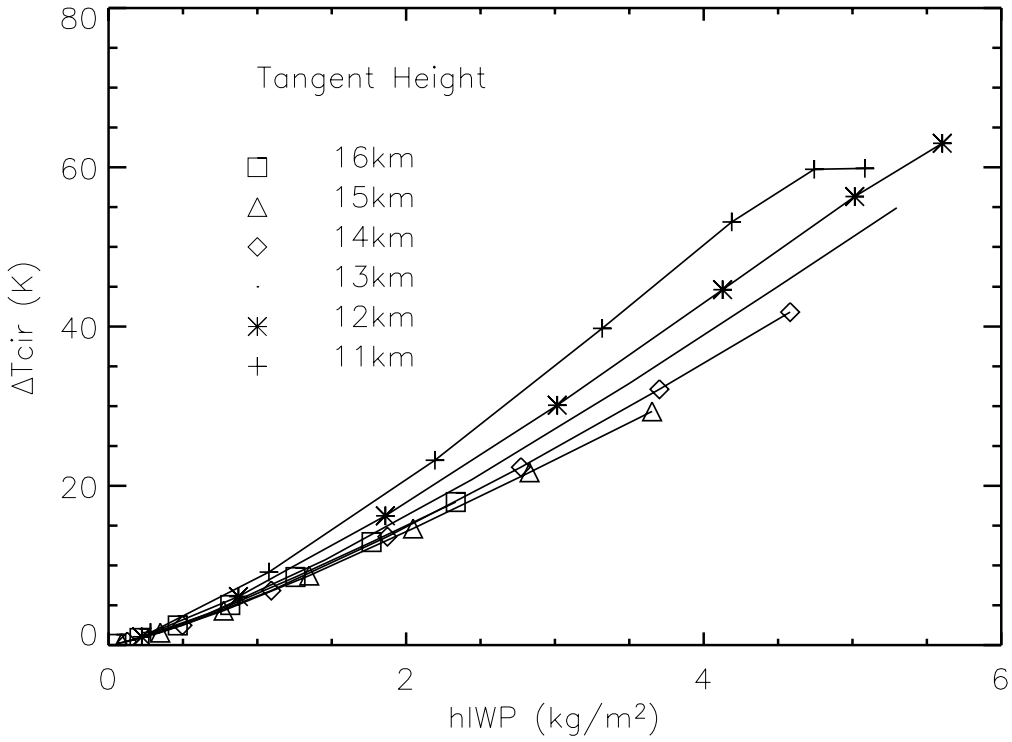

Figure 13. Cloud ice, water vapor and temperature maps at 100 hPa for January-March 1992. Top: MLS cloud occurrence frequency (colors) and NCEP temperature (contours). Middle: MLS *IWC* (colors) and H_2O *vmr* (contours). Bottom: MLS *IWC* (colors) and RH_i (contours). Profiles contaminated by clouds are excluded in the water vapor and RH_i maps.

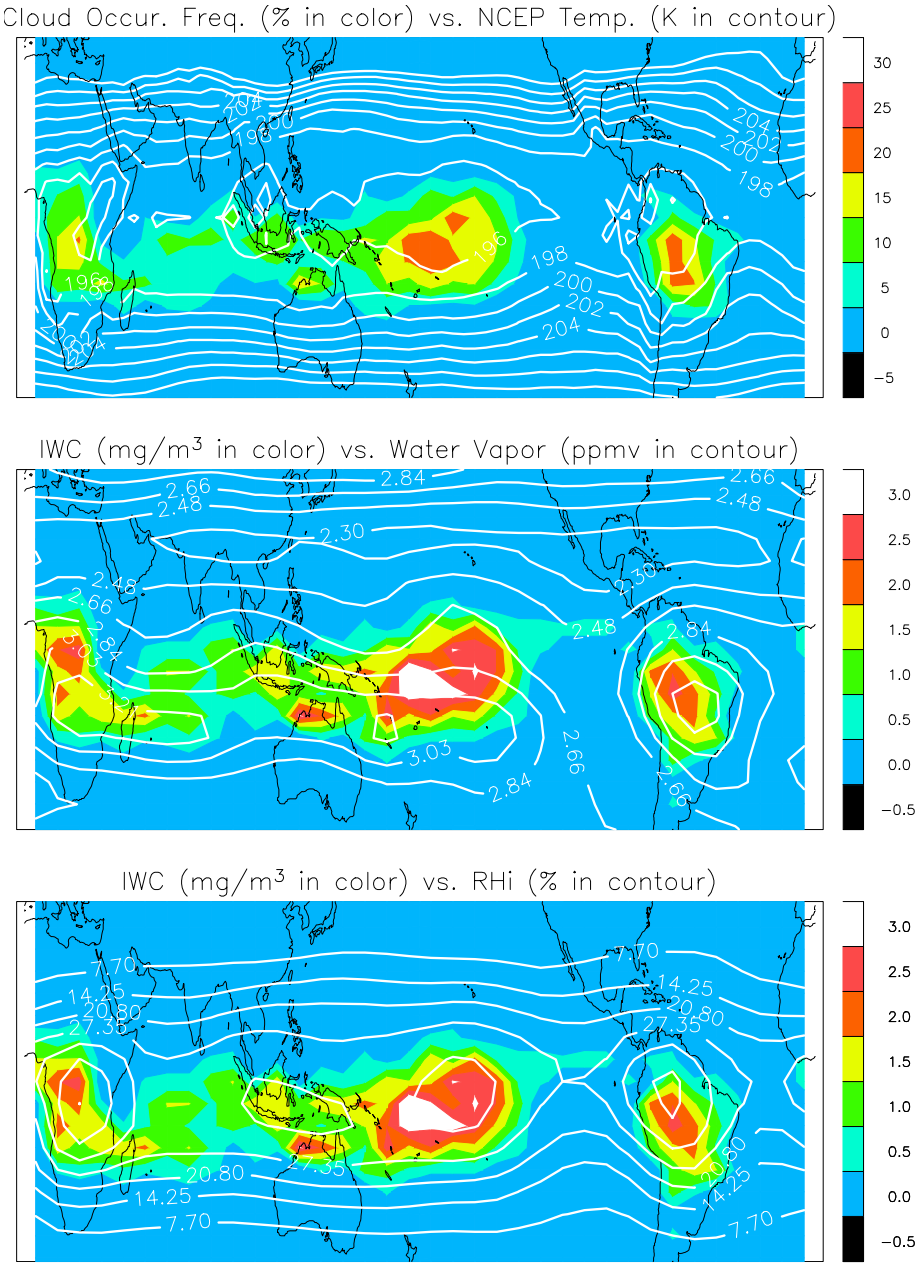

Figure 14. As in Figure 5 except for July-September 1992.

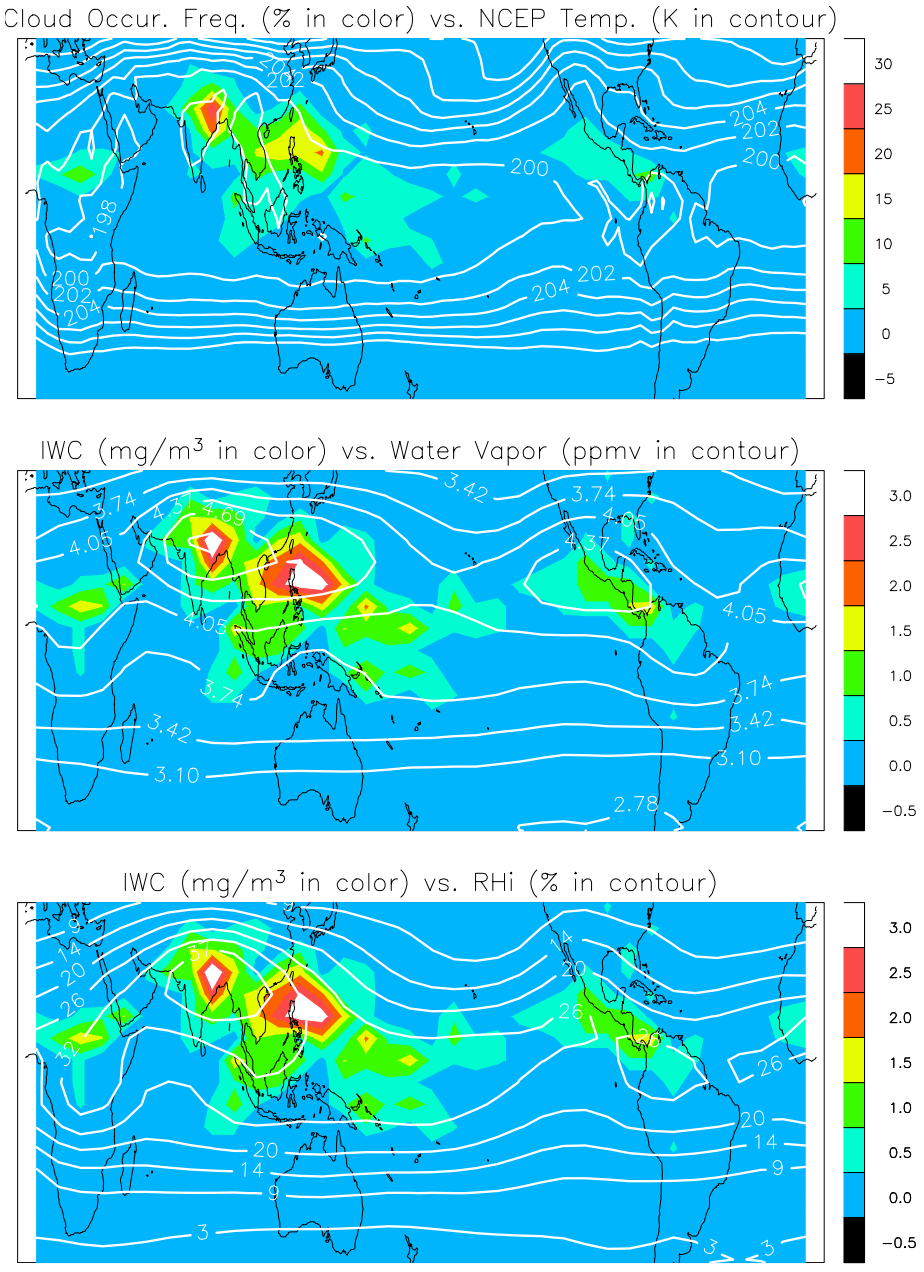

Figure 15. The time series of (a) 100-hPa MLS cloud radiance, (b) 146-hPa MLS H_2O *vmr*, (c) 100-hPa MLS H_2O *vmr*, and (d) 100-hPa MLS RH_i,. The cloud radiance is used to estimate *IWC* variations at 100 hPa. As described in section 3, the radiance can be approximately converted to 100-hPa *IWC* using the factor of 0.15 mg/m^3/K. For the 100-hPa H_2O *vmr* and *RHi* results, cloudy profiles are excluded from the averaging. The white strips represent missing data. In the *RHi* time series, sudden increases/decreases in value are likely the retrieval errors as *RHi* becomes very sensitive to temperature uncertainty at this level.

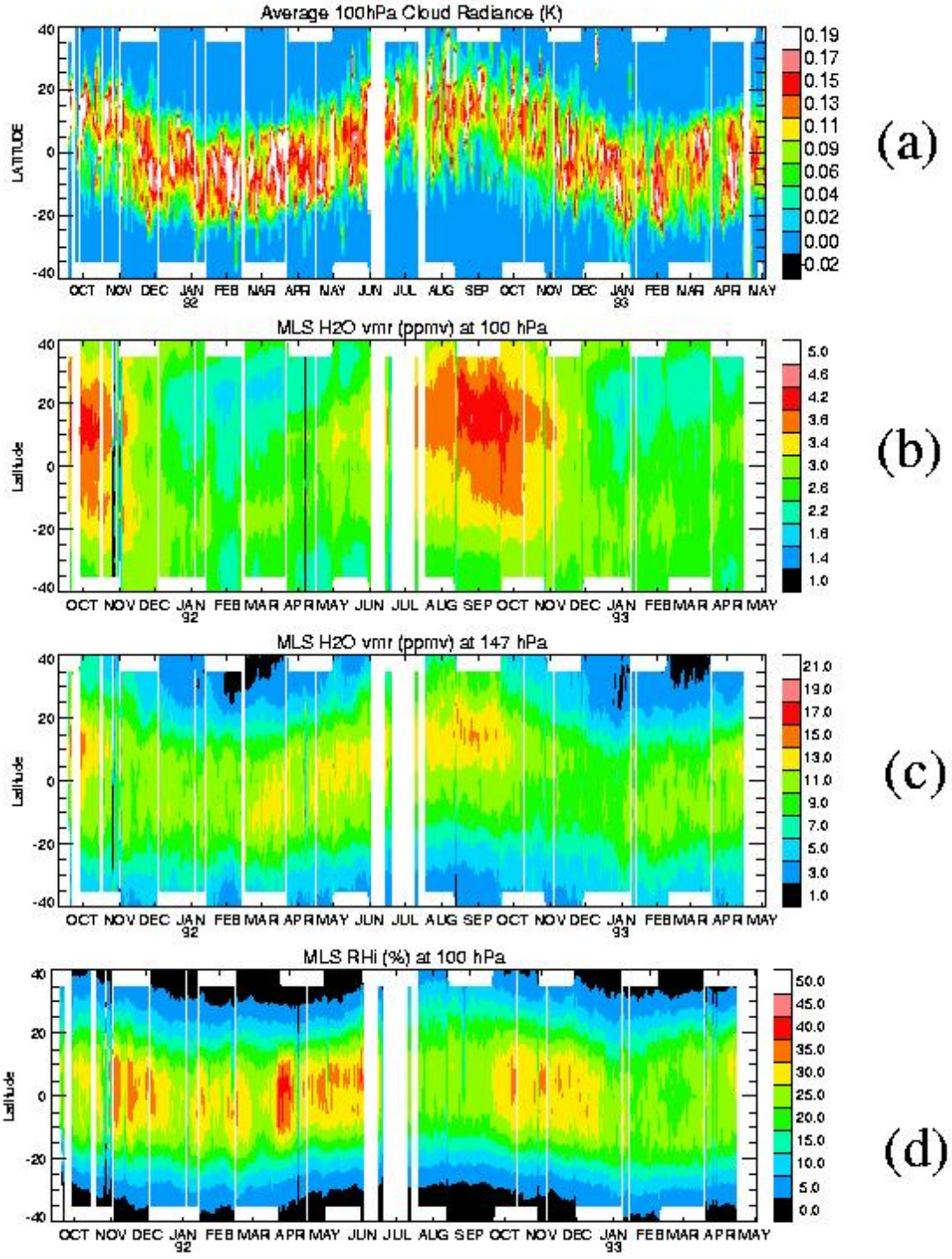

Figure 16. Average (30°S-30°N) MLS cloud radiances at 100 and 130 hPa tangent pressures during 1991-1997. Daily averages are plotted in small dots whereas the 30-day running averages are represented by large dots. Interpolation is applied to obtain the values at 100 and 130 hPa. Data are excluded if the number of measurements is less than 200 in the latitude bin.

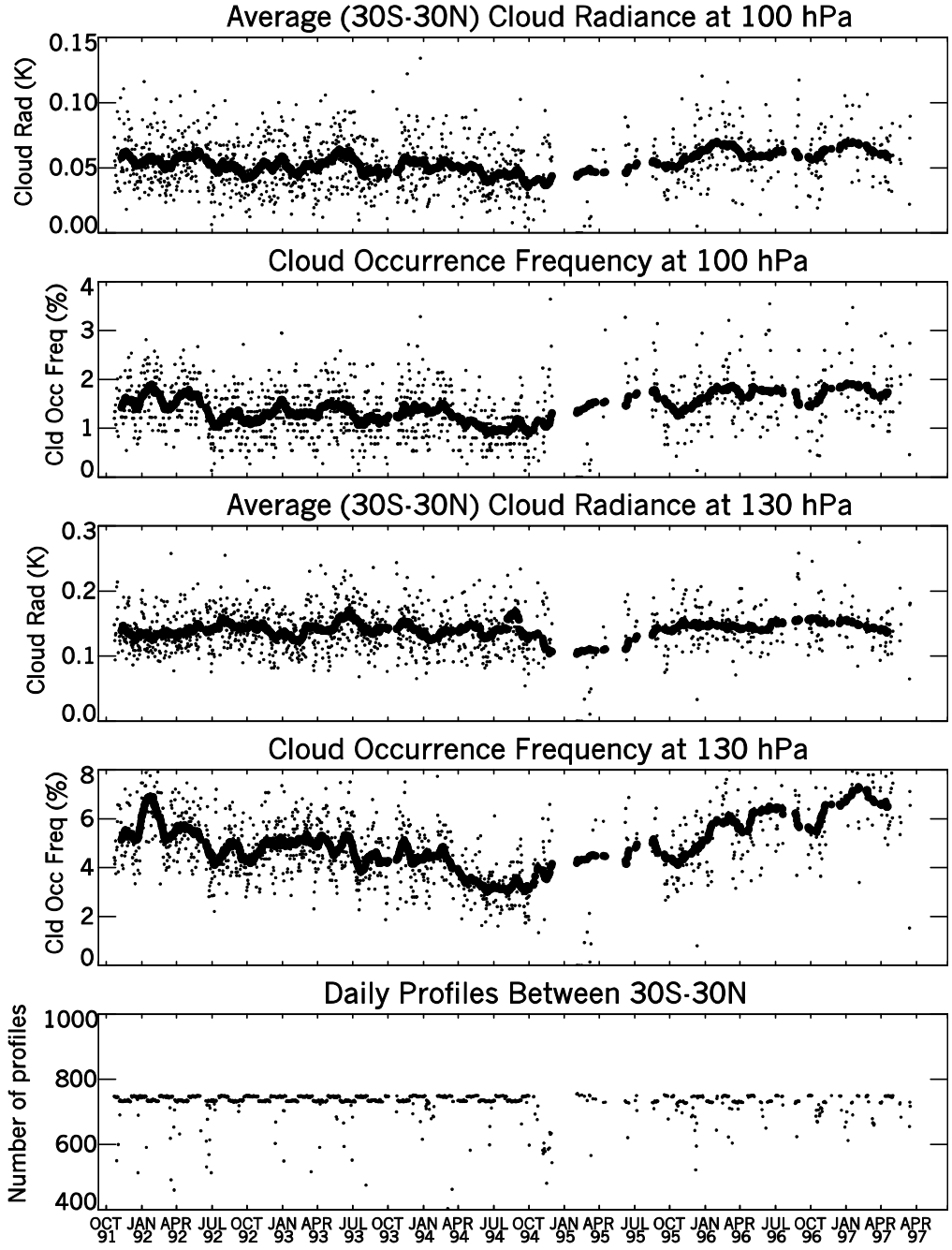

Figure A.1 Diagram to illustrate the geometry of cloud scattering calculation in the limb RT model.

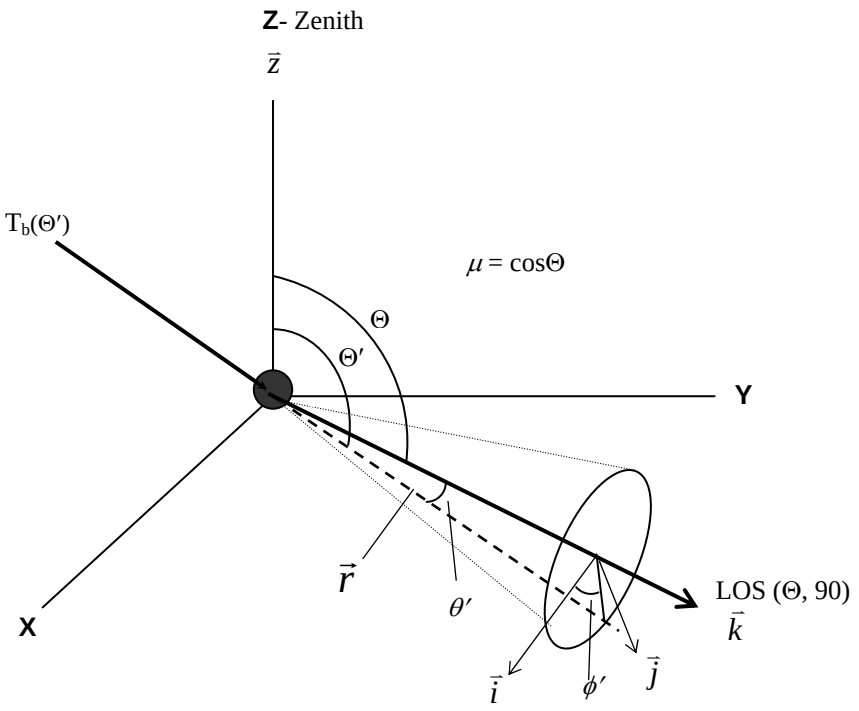

Figure A.2. Calculated IWC-ΔT_{cir} relation at 100 hPa. The dotted line shows the slope of 1.5 mg/m^3/K in the linear portion of the IWP-ΔT_{cir} relation.